Research article

Christina Bauer and Harald Giessen*

Tailoring the plasmonic Fano resonance in metallic photonic crystals

https://doi.org/10.1515/nanoph-2019-0335
Received August 30, 2019; revised December 16, 2019; accepted January 8, 2020

Abstract: Periodically arranged metallic nanowires on top of a waveguide layer show a strong coupling between the particle plasmon of the wires and the waveguide mode. By introducing a dielectric spacer layer between the metallic structures and the waveguide layer, this coupling can be reduced. Here, the thickness of this spacer layer is varied and the coupling strength is determined for each spacer layer thickness by fitting an effective energy matrix to the energy positions of the resonance peaks. It is found that the coupling strength can be very well described by the electric field amplitude of the waveguide mode at the location of the nanowires. We carried out experiments and found very good agreement with theory and our simple model. Using this method, we achieved experimentally an extremely small mode splitting as small as 25 meV leading to very sharp spectral features. Our pathway and design for tailoring the coupling strength of plasmonic Fano resonances will enable the design of highly sensitive plasmonic sensor devices and open the door for narrow plasmonic spectral features for nonlinear optics and slow light propagation.

Keywords: coupling strength; Fano resonance; photonic crystals; plasmonic; waveguide.

1 Introduction

Coupling between plasmonic modes and electromagnetic radiation has attracted the interest of many researchers in the recent years. Using this effect, it is possible to enhance the fluorescence of molecules [1, 2], vibrational signal of molecules [3, 4], magneto-optical effects in thin films [5–7], and efficiency of solar cells [8–11] and light-emitting diodes [12–14]. Plasmonic coupling has also been used for refractive index sensing [15–17], biosensing [18–21], and gas sensing [22–25]. One example of gas sensing is the detection of the hydrogen content in air [26–29]. This is very important, as already a hydrogen concentration of 4% in air can lead to spontaneous combustion and explosion. For the purpose of sensing, a very narrow extinction dip is desired, as such a sharp feature increases the sensitivity tremendously [30, 31]. Therefore, it is crucial to be able to tune the coupling strength between the plasmonic resonance and the photonic resonance. In the study of Zentgraf et al. [32], gold wires were embedded within a waveguide, and it has theoretically been shown that the coupling strength between the particle plasmon resonance and the waveguide mode follows the electric field amplitude of a transverse magnetic waveguide mode within the waveguide. However, it is quite important to place the metallic wires outside the waveguide for sensing purposes using a spacer layer of specific thickness between the wires and the waveguide, which should reduce the coupling between these two oscillators and narrow down the Fano resonance features. In this paper, we fabricated samples with different spacer layer thicknesses and determined the corresponding coupling strengths. It is found that the coupling strength can indeed be tuned using this approach. By comparing different sensor designs for hydrogen sensing, it is found that a spacer layer sensor will be superior to a sensor with embedded wires.

2 Results and discussion

In the first part of the paper, the influence of a spacer layer between a gold grating and a slab waveguide is examined experimentally and theoretically. The samples in this study consist of a glass substrate with an indium-tin-oxide (ITO) waveguide layer of 140 nm thickness and a gold grating on top (see Figure 1). The metal wires possess a width of 100 nm, a height of 20 nm, and a length of 100 μm with a grating period d_x varying between 300 and 500 nm in steps of 50 nm. A silicon dioxide (SiO_2) spacer

***Corresponding author: Harald Giessen,** 4th Physics Institute and Research Center SCoPE, University of Stuttgart, 70550 Stuttgart, Germany, e-mail: h.giessen@pi4.uni-stuttgart.de
Christina Bauer: 4th Physics Institute and Research Center SCoPE, University of Stuttgart, 70550 Stuttgart, Germany

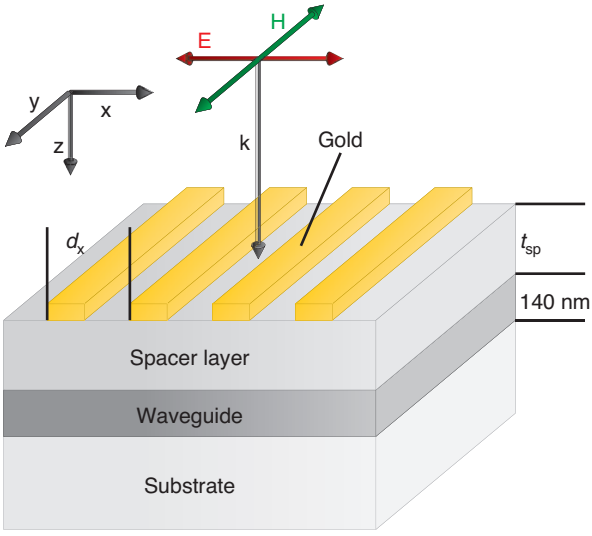

Figure 1: Schematic view of the sample structure.
The thickness t_{sp} of the spacer layer (SiO_2) between the 140-nm-thick waveguide layer (ITO) and the periodic gold grating is varied between 0 and 350 nm in steps of 50 nm. The grating period d_x is varied between 300 and 500 nm.

layer with a specific thickness t_{sp} is located between the waveguide slab and the gold grating. To influence the optical properties of such metallic photonic crystals, t_{sp} is varied between 0 and 350 nm in steps of 50 nm. The experiments will be verified by a theoretical model. The results of the first part of the paper will be used to develop sensor designs for hydrogen sensing in the second part of the paper.

The measured spectra are shown as black solid curves for spacer layer thicknesses $t_{sp}=0$, 100, 200, and 300 nm in Figure 2A–D, respectively. The corresponding simulated spectra, calculated using the scattering-matrix formalism [33, 34], are plotted as red dashed curves with the parameters mentioned in Methods. The agreement between the measured and simulated spectra is quite good. The major difference is the height of the particle plasmon resonance. The decreased height of the experimental spectra might be due to inhomogeneous broadening and additional material damping in the gold. The spectra with $d_x=300$ nm are shown on top in each panel and those with $d_x=500$ nm are shown at the bottom. For the sample without spacer layer (see Figure 2A), the optical properties can be understood as follows. The polarized light excites a particle plasmon in gold nanostructures leading to a broad resonance in the extinction spectrum [35]. This can be seen as the lower energy resonance in the spectrum for $d_x=300$ nm. The resonance on the higher energy side is the waveguide mode, i.e. light coupled into the waveguide slab by periodic grating [35]. This waveguide mode is strongly dependent on the grating period leading to a shift of this resonance to lower energies for larger grating periods. Due to the strong interaction between particle plasmon and waveguide mode, an anticrossing behavior can be recognized [36]. A new quasiparticle is formed, the so-called waveguide-plasmon polariton [36]. When a spacer layer is introduced between the ITO waveguide layer and the gold grating, it can obviously be seen that the particle plasmon resonance is shifted to higher energies (see Figure 2). This can be explained by the different dielectric surrounding of the gold structures. The change of the refractive index from a high value (n_{ITO} for $t_{sp}=0$ nm) to a low value (n_{sp} for $t_{sp}\neq 0$ nm) results in a shift to higher energies [37, 38]. An additional impact of the spacer layer thickness to the optical properties is the reduction of the spectral distance between the two polariton branches. By looking at the spectra in the center of Figure 2B–D corresponding to the grating period $d_x=400$ nm, one can recognize this decreased spectral distance. This behavior can be understood by considering the electric fields of the two modes. The electric field of the particle plasmon is mainly located at the positions of the gold wires [39], whereas the electric field E_x of the waveguide mode is concentrated within the waveguide slab with an exponential decay in the surrounding material [40]. By looking at the spatial overlap between the two electric fields, one observes that this overlap decreases for increasing distances between the gold wires and the waveguide slab. As the coupling strength between the waveguide mode and the particle plasmon is dependent on this spatial overlap [32], an increased spacer layer thickness results in a decreased coupling strength and thus in a reduced spectral distance between the two polariton branches.

To verify this assumption, the energy positions of the extinction maxima extracted from the measured spectra in Figure 2 are depicted in Figure 3 as a function of grating period for spacer layer thicknesses (a) $t_{sp}=0$ nm, (b) $t_{sp}=100$ nm, (c) $t_{sp}=200$ nm, and (d) $t_{sp}=300$ nm. This anticrossing behavior possesses a reduced polariton splitting ΔE for an increased spacer layer thickness. To describe the anticrossing behavior, the effective energy matrix E_{eff} of Ref. [36] for normal incidence ($k_x=0$) and with neglected spectral widths is assumed as follows:

$$E_{eff}=\begin{pmatrix} E_{wg}(d_x)+V_1 & \sqrt{2}V_2 \\ \sqrt{2}V_2 & E_{Pl} \end{pmatrix}. \quad (1)$$

Here, E_{wg} is the normal incidence waveguide mode energy dependent on the grating period d_x, E_{pl} is the energy of the particle plasmon, and V_2 is the coupling

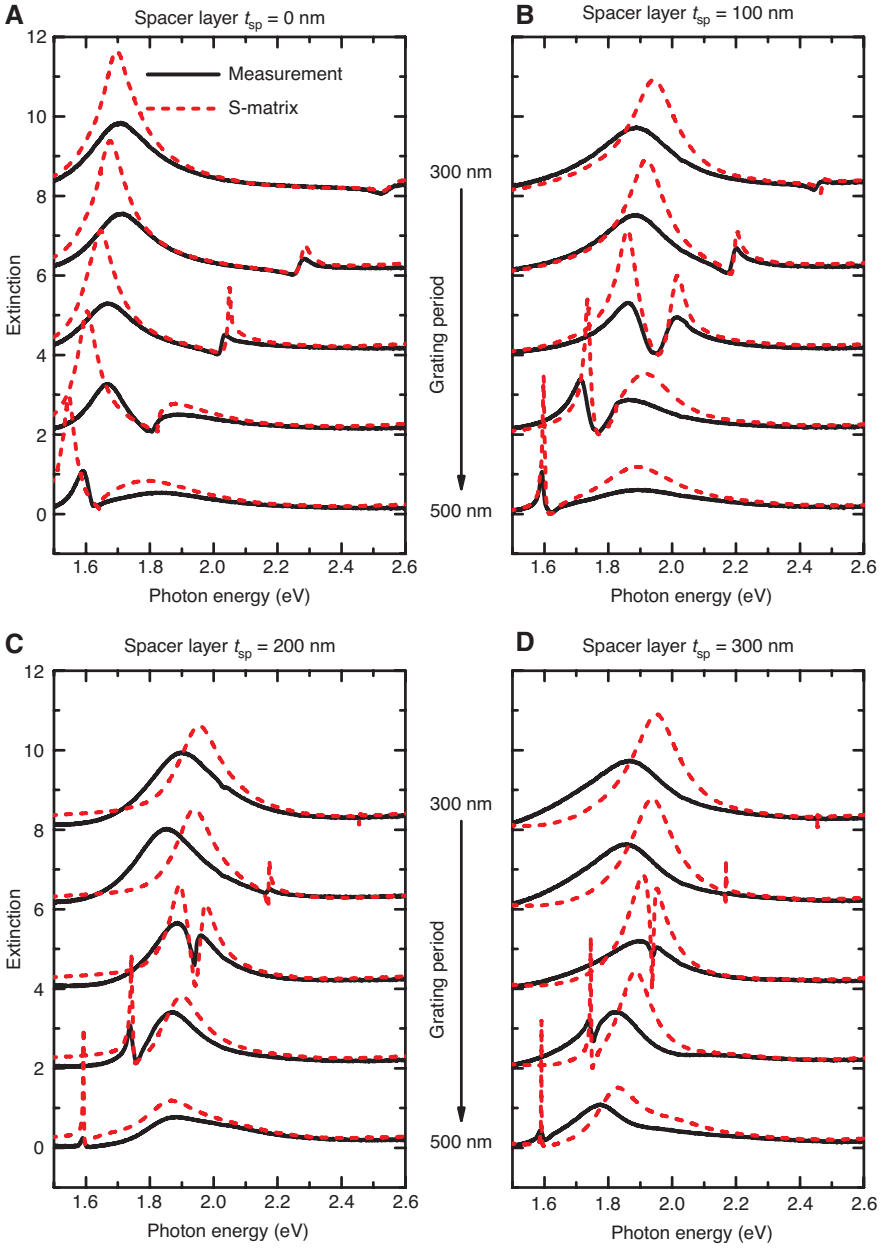

Figure 2: Coupling strength behavior for different spacer layer thicknesses.
Measured (black solid) and simulated (red dashed) extinction spectra for spacer layer thicknesses t_{sp} of (A) 0 nm, (B) 100 nm, (C) 200 nm, and (D) 300 nm. The grating period is varied between 300 nm (top) and 500 nm (bottom) in steps of 50 nm for each panel. The spectra are shifted upward for clarity in each panel.

strength between the two resonances. For the half-width of the photonic band gap V_1, a value of 20 meV is assumed. The eigenenergies of Equation (1) given by

$$E_{1/2} = \frac{E_{wg} + V_1 + E_{Pl} \pm \sqrt{(E_{wg} + V_1 - E_{Pl})^2 + 8V_2^2}}{2} \quad (2)$$

are plotted as red lines in Figure 3. The only free parameter in Equation (2) is the coupling energy V_2, which is fitted to the individual data sets of Figure 3. Using this method, V_2 is identified for all spacer layer thicknesses for the measured and simulated data. The polariton splitting is obtained by calculating the minimum energy difference between the top and bottom polariton branches. As the minimum energy difference is obtained for $E_{wg} = E_{Pl} - V_1$, ΔE is given by

$$\Delta E = E_1 - E_2 = 2\sqrt{2}V_2. \quad (3)$$

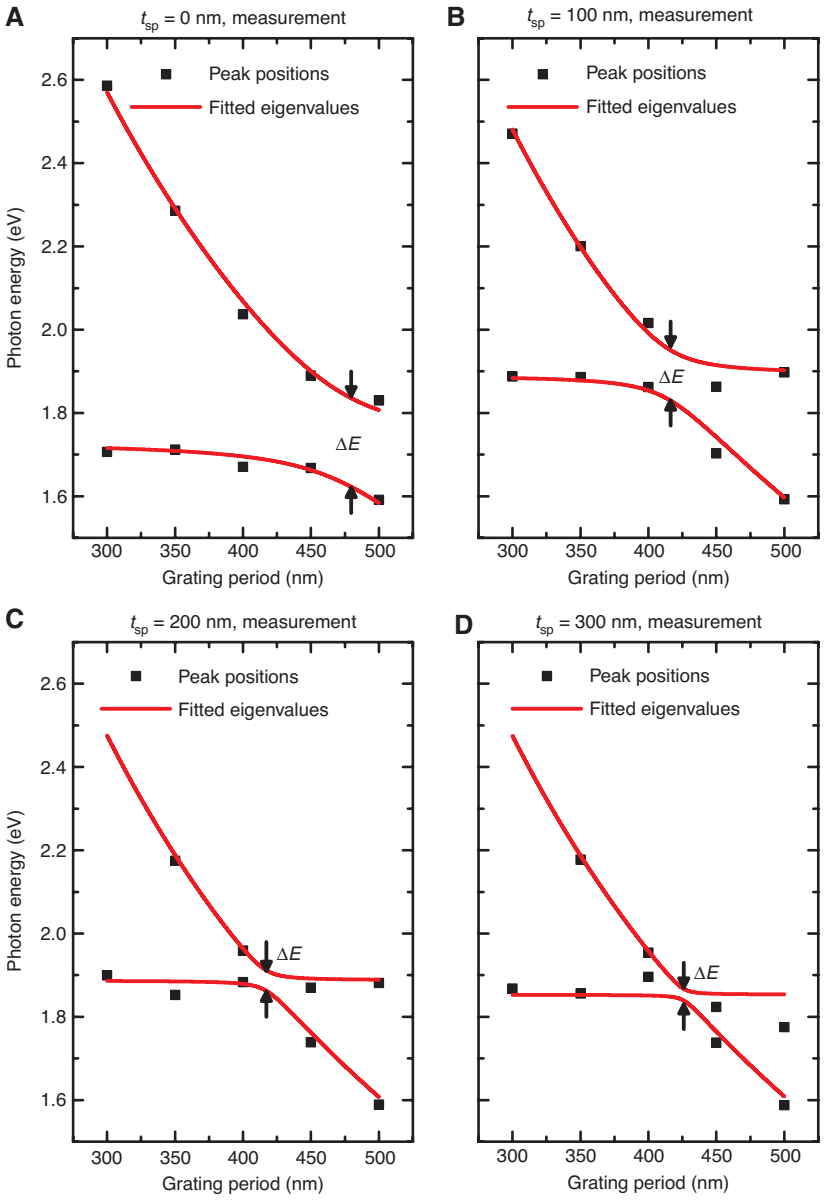

Figure 3: Coupling strength behavior for different spacer layer thicknesses.
Energy positions of the extinction maxima versus grating period d_x extracted from the measured spectra (black squares) for (A) $t_{sp} = 0$ nm, (B) $t_{sp} = 100$ nm, (C) $t_{sp} = 200$ nm, and (D) $t_{sp} = 300$ nm. Red lines correspond to the fitted eigenvalues of the effective energy matrix [Equation (1)].

The polariton splitting thus obtained is depicted as a function of spacer layer thickness in Figure 4A (left scale) with the black squares corresponding to the measured data and the red circles to the simulated data. The normalized electric field amplitude $|E_x|$ of a transverse magnetic waveguide mode (see inset) is plotted in this figure versus the corresponding spacer layer thickness as the green solid line (right scale). To calculate E_x, an undisturbed waveguide slab without grating coupler sandwiched between a cover and a substrate layer is assumed with the electric field decaying exponentially in the two surrounding layers. The vertical dependence of the field amplitude E_x as a function of z is depicted in Figure 4B for an exemplary spacer layer thickness of $t_{sp} = 200$ nm. For the thickness and the refractive indices, the parameters given in Methods for the scattering matrix calculations are used. The propagation constant β_p was assumed to possess the value $\beta_p \approx 1.571 \times 10^7$ m^{-1}. A similar behavior of the polariton splitting (circles and squares) and the electric field amplitude (green line) can be recognized in Figure 4A. The agreement between the simulated data and the electric field amplitude is particularly good. The deviations of the measured splitting to the simulations might be due to slightly different spacer layer thicknesses or sample imperfections. This good agreement between the behavior of the polariton

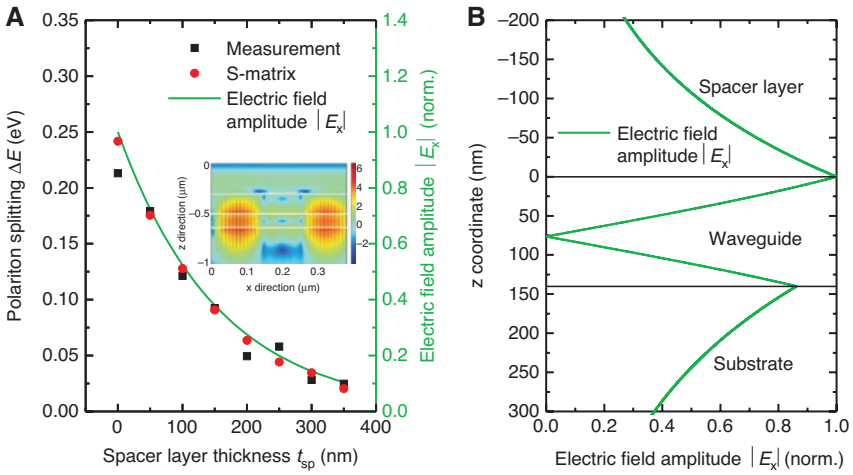

Figure 4: Correlation between polariton splitting and electric field amplitude.
(A) Polariton splitting ΔE as a function of spacer layer thickness t_{sp} for experimental data (black squares) and simulated data (red circles) compared to the normalized electric field amplitude $|E_x|$ (green line) at the vertical position of the metal grating as a function of spacer layer thickness for a propagation constant $\beta_p \approx 1.571 \times 10^7\ m^{-1}$. Inset: field plot for E_x (transverse cross-section) at $E = 1.935$ eV. (B) Exemplary $|E_x|$ field plot of an undisturbed waveguide mode as a function of the vertical coordinate z for a spacer layer thickness of 200 nm.

splitting and the behavior of the electric field amplitude proves our assumption of the electric field overlap between particle plasmon and undisturbed waveguide mode to be responsible for the polariton splitting. To use this model to tune the coupling between a particle plasmon and a waveguide mode, it is necessary to adjust the parameters to the specific dielectric surrounding. The waveguide can be any material with a larger refractive index than the surrounding materials. The substrate and spacer layer can also be any material with a lower refractive index than the waveguide. This layer can even be a nanostructured layer with an average refractive index. The cross-section, the grating period, and the waveguide thickness need to be adjusted to tune the resonances to a specific energy position, e.g. the energy of a used laser. Last but not least, the coupling between the two resonances can be tuned by choosing a specific spacer layer thickness.

Such a configuration with a specific spacer layer thickness can be used for sensing devices, making use of a very narrow extinction dip within the plasmon resonance [17, 41, 42]. For gas sensing, it is important to use materials that are sensitive to the specific gas. As tungsten oxide (WO_3) has a high refraction index and is a hydrogen-sensitive material, as it changes its optical properties for different hydrogen concentrations due to the gasochromic effect [43, 44], it is used as a waveguide material instead of ITO. Using the results of the first part of this paper, three different designs for such a hydrogen sensor are compared theoretically (see Figure 5). A 250-nm-thick WO_3 layer serves as waveguide layer in all three cases. In all three designs, a gold grating of 425 nm

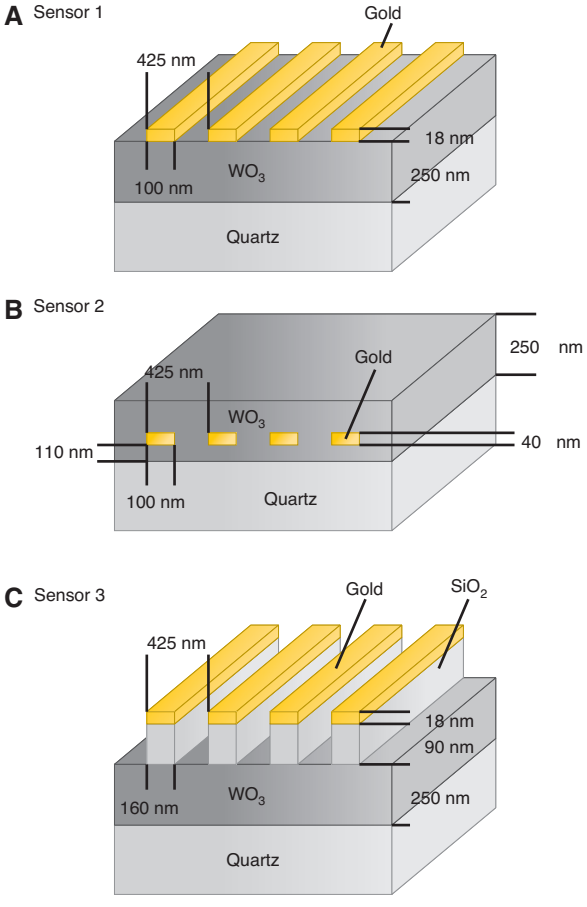

Figure 5: Three different sensor designs.
Hydrogen sensor design with (A) the gold wires directly on top of the 250-nm-thick WO_3 waveguide, (B) the gold wires embedded within the 250-nm-thick WO_3 waveguide, and (C) the gold wires separated from the 250-nm-thick WO_3 waveguide by introducing SiO_2 wires as spacer layer.

period is used. However, the location of the grating is different in the three cases. Figure 5A shows a design where the gold grating is directly placed on top of the waveguide layer. In the next design, the gold grating is embedded within the waveguide layer (see Figure 5B). Such a design was proposed by Zentgraf et al. [32] to be suitable for sensing. In the last design, the gold grating is placed on top a SiO_2 spacer layer (see Figure 5C). However, if a continuous SiO_2 spacer layer was used, hydrogen would not be able to reach and penetrate the WO_3 layer. Thus, the optical properties of the WO_3 could not be changed, which means that such a device would not be suitable for sensing. Therefore, a nanostructured SiO_2 layer with the same grating period as the gold grating is used as spacer. In this case, an average refractive index of SiO_2 and air has to be considered, leading to a smaller refractive index than a continuous SiO_2 layer. However, this does not matter, as the average refractive index is still lower than the refractive index of the waveguide layer. The important point is that the average refractive index has to be used in the theoretical model. As the dielectric surrounding of the gold wires is different for the three designs, it is crucial to change the cross-section of the gold wires to ensure the particle plasmon to be at approximately the same resonance energy in all three cases. The first design uses a gold wire cross-section of 100×18 nm (see Figure 5A), the second design uses a cross-section of 100×40 nm (see Figure 5B), and the third design uses a cross-section of 160×18 nm (see Figure 5C). To tune the sensor parameters and have an idea how narrow the resonances within the plasmon resonance will be, we take into account the electric field amplitude within the three layers. The electric field amplitude in the substrate and in the waveguide layer will be the same for all three sensor designs. However, the exponential decay in the cover layer of the first two designs will be in air, whereas that of the third design will be in a material with an average refractive index of SiO_2 and air. As the gold gratings in the first design are placed directly on the top of the waveguide layer where the electric field amplitude is highest, a large coupling is expected. For the next two designs, the coupling is lower, leading to narrower resonances within the particle plasmon. To have a comparable coupling strength in these two designs, the gold wires of design 2 are placed with a distance of 110 nm above the substrate and the wires of design 3 on top of a 90-nm-thick nanostructured SiO_2 spacer layer.

The simulated extinction spectra for sensors 1–3 are displayed in Figure 6A–C, respectively. The spectra were calculated for different injected charge densities using the scattering-matrix method mentioned in Methods. For the spectra without injected charge density (black solid lines), one can see that the coupling between the two resonances is comparable for sensors 2 and 3 (Figure 6B and C) but larger for sensor 1 (Figure 6A) as expected due to the larger coupling strength. In all three sensor designs, an extinction dip is still visible for an injected charge density of 11 mC cm^{-2} μm^{-1} (red dashed lines). However, the minimum is not that pronounced anymore due to the increase of the imaginary refractive index of WO_3. Additionally, the extinction minimum is shifted to higher energies due to the decrease of its real refractive index. As the gold wires are in direct contact to the WO_3 for sensors 1 and 2, the particle plasmon resonance is broadened and shifted to higher energies. Only for sensor 3, where the gold wires are separated from the WO_3 layer, the particle plasmon remains constant in its spectral width and energy position. This is because the dielectric surrounding of the gold wire stays the same only for this sensor. This behavior continues as the injected charge density is increased.

One possibility of a sensor design is that a monochromatic laser detects the extinction at its specific wavelength. Therefore, the energy at the extinction minimum for 0 mC cm^{-2} μm^{-1} is identified and the extinction values for all injected charge densities are observed for this energy (see vertical lines in Figure 6A–C). Note that the energy is comparable in all three cases but not identical. The evaluation is done this way so that it is possible to detect the maximum possible sensing result for each design. To design such a sensor for real applications, the particle plasmon and the waveguide mode have to be tuned to the laser wavelength for maximum sensing results. The extinction values obtained in this way are plotted versus the corresponding injected charge density for sensor 1 (black squares), sensor 2 (red circles), and sensor 3 (green triangles) in Figure 6D. Sensor 3 shows the highest difference in extinction values and thus also the largest sensitivity due to the constant spectral width and energy position of the particle plasmon resonance. The reason is that the spacer layer creates a dielectric surrounding around the gold wires that is independent from the injected charge density. This means that the best sensor design of these three sensors is actually the one with the spacer layer. Although the extinction spectra for 0 mC cm^{-2} μm^{-1} injected charge density is comparable for sensors 2 and 3, the separation of gold wires and WO_3 layer in sensor design 3 leads to a better sensitivity.

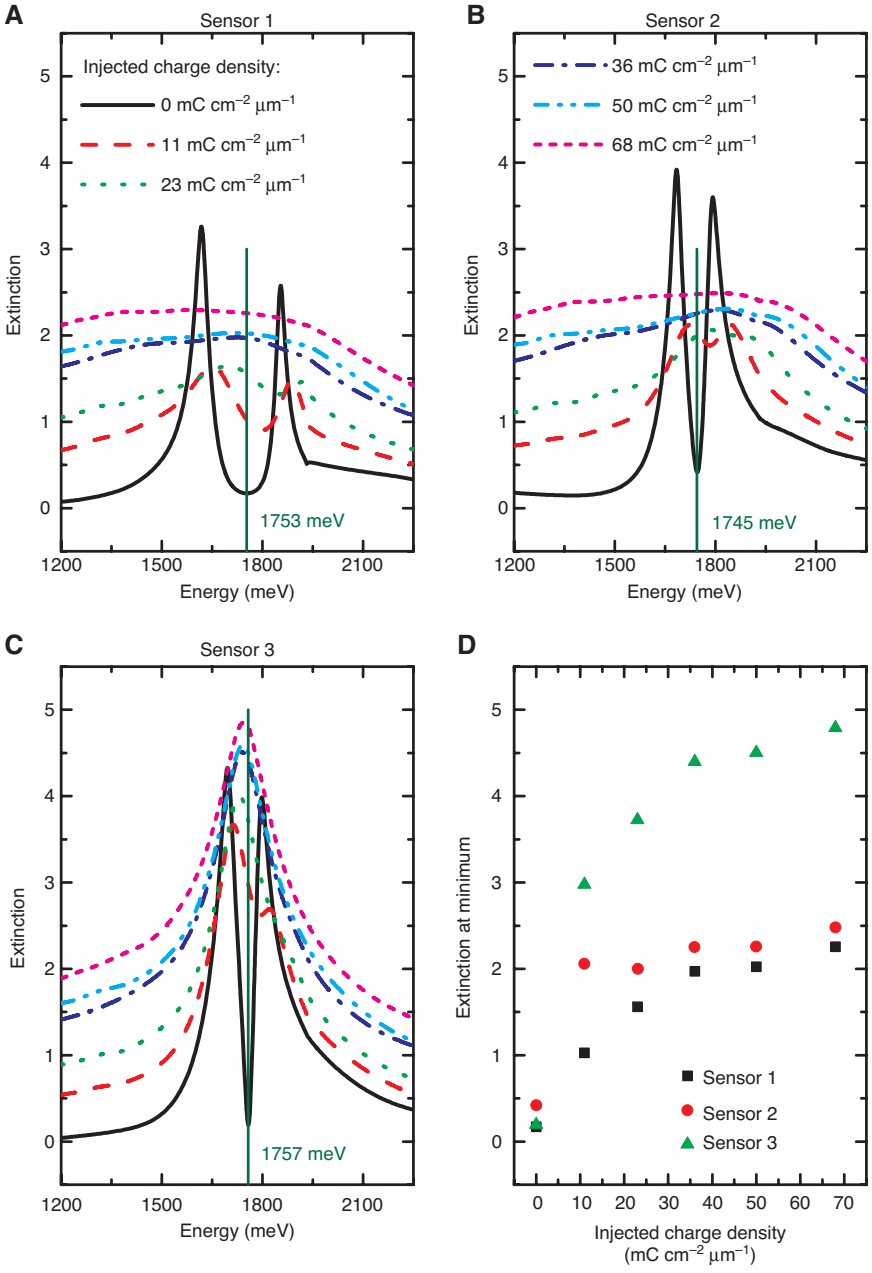

Figure 6: Performance of three different sensor designs.
Calculated extinction spectra for different injected charge densities for (A) sensor design 1, (B) sensor design 2, (C) sensor design 3, and (D) Extinction values at the extinction minimum are plotted versus the injected charge density for the three sensor designs.

3 Conclusions

We have shown that the coupling strength of a metallic photonic crystal can be controlled by varying the thickness of a spacer layer between the gold grating and the waveguide layer. It is found that the coupling strength is linearly dependent on the electric field amplitude E_x of the waveguide mode. For large spacer layer thicknesses, very narrow extinction dips can be found that can be used for sensing devices. With the help of these results, it was possible to design three different designs for hydrogen sensing with two of the designs having comparable coupling strengths. It is found that the sensor using the spacer layer is superior to the other two designs due to a dielectric surrounding of the gold wires independent from the injected charge density. Our pathway and design for tailoring the coupling strength of plasmonic Fano resonances will enable the design of highly sensitive plasmonic sensor devices and open the door for narrow plasmonic spectral features for nonlinear optics and slow light propagation.

4 Methods

The samples were fabricated by evaporating the desired thickness t_{sp} of SiO_2 onto the ITO substrate. The gold gratings in arrays of 100×100 μm² were placed on top of the spacer layer using electron beam lithography. These samples were mounted in the focus of a microscope objective (Zeiss, A-Plan, 10×, NA = 0.25) with linearly polarized white light as the light source. The light was normally incident on the sample with the polarization perpendicular to the wires (see Figure 1). After recollimation of the beam behind the sample, a pinhole with a 100 μm diameter was taken to ensure a beam aperture angle of below 0.2° (Ref. [36]). Finally, the beam was focused onto the slit of a spectrometer (Acton Spectra Pro 500i), in which a grating with 150 lines/mm was used. The spectra were taken using a CCD camera controlled by a computer program.

The simulated spectra were calculated using a scattering-matrix method [33, 34]. For the refractive indices of the glass substrate and the SiO_2 spacer layer, the constant values $n_{sub} = 1.51$ and $n_{sp} = 1.46$ were assumed. The measured values of Johnson and Christy [45] were used for the optical constants of gold and the refractive index of ITO can be described by Cauchy's equation:

$$n_{ITO} = 1.83284 + \frac{0.04435}{\lambda^2} - \frac{0.00089}{\lambda^4} \quad (4)$$

where λ is the wavelength of the incident light in μm. For the refractive index of various injected charge densities in WO_3 corresponding to the injected hydrogen contents, the values given in Ref. [46] were used. For the gold wires in the simulations of the ITO samples, a cross-section of 105×17 nm² was taken, which was slightly different than the experimentally found value. However, the experimental determination of these values included uncertainties leading to deviations between measurement and theory [47]. Thus, this adjustment resulted in a better agreement between experimental and calculated spectra [47].

Acknowledgments: The authors thank T. Weiss for providing his scattering-matrix code for the simulations. The work was financially supported by Deutsche Forschungsgemeinschaft (grant SPP1391, Funder Id: http://dx.doi.org/10.13039/501100001659), by Baden-Württemberg-Stiftung, and by Bundesministerium für Bildung und Forschung (grants 13N9155 and 13N10146, Funder Id: http://dx.doi.org/10.13039/501100002347). We acknowledge funding by DFG (Open Access Funds) and ERC (ComplexPlas).

References

[1] Tam F, Goodrich GP, Johnson BR, Halas NJ. Plasmonic enhancement of molecular fluorescence. Nano Lett 2007;7:496–501.
[2] Teng Y, Ueno K, Shi X, Aoyo D, Qiu J, Misawa H. Surface plasmon-enhanced molecular fluorescence induced by gold nanostructures. Ann Phys 2012;524:733–40.
[3] Neubrech F, Pucci A, Cornelius TW, Karim S, García-Etxarri A, Aizpurua J. Resonant plasmonic and vibrational coupling in a tailored nanoantenna for infrared detection. Phys Rev Lett 2008;101:157403.
[4] Pryce IM, Kelaita YA, Aydin K, Atwater HA. Compliant metamaterials for resonantly enhanced infrared absorption spectroscopy and refractive index sensing. ACS Nano 2011;5:8167.
[5] Belotelov VI, Akimov IA, Pohl M, et al. Enhanced magneto-optical effects in magnetoplasmonic crystals. Nat Nanotechnol 2011;6:370–6.
[6] Chin JY, Steinle T, Wehlus T, et al. Nonreciprocal plasmonics enables giant enhancement of thin-film Faraday rotation. Nat Commun 2013;4:1599.
[7] Kreilkamp LE, Belotelov VI, Chin JY, et al. Waveguide-plasmon polaritons enhance transverse magneto-optical Kerr effect. Phys Rev X 2013;3:041019.
[8] Rockstuhl C, Fahr S, Lederer F. Absorption enhancement in solar cells by localized plasmon polaritons. J Appl Phys 2008;104:123102.
[9] Munday JN, Atwater HA. Large integrated absorption enhancement in plasmonic solar cells by combining metallic gratings and antireflection coatings. Nano Lett 2011;11:2195–201.
[10] Ferry VE, Verschuuren MA, van Lare MC, Schropp REI, Atwater HA, Polman A. Optimized spatial correlations for broadband light trapping nanopatterns in high efficiency ultrathin film a-Si:H solar cells. Nano Lett 2011;11:4239–45.
[11] Bauer C, Giessen H. Light harvesting enhancement in solar cells with quasicrystalline plasmonic structures. Opt Express 2013;21:A363–71.
[12] Kwon MK, Kim JY, Kim BH, et al. Surface-plasmon-enhanced light-emitting diodes. Adv Mater 2008;20:1253–7.
[13] Koo WH, Youn W, Zhu P, Li XH, Tansu N, So F. Light extraction of organic light emitting diodes by defective hexagonal-close-packed array. Adv Funct Mater 2012;22:3454–9.
[14] Gao N, Huang K, Li J, Li S, Yang X, Kang J. Surface-plasmon-enhanced deep-UV light emitting diodes based on AlGaN multi-quantum wells. Sci Rep 2012;2:816.
[15] Liu N, Mesch M, Weiss T, Hentschel M, Giessen H. Infrared perfect absorber and its application as plasmonic sensor. Nano Lett 2010;10:2342–8.
[16] Zhao J, Zhang C, Braun PV, Giessen H. Large-area low-cost plasmonic nanostructures in the NIR for Fano resonant sensing. Adv Mater 2012;24:OP247–52.
[17] Gallinet B, Martin OJF. Refractive index sensing with subradiant modes: a framework to reduce losses in plasmonic nanostructures. ACS Nano 2013;7:6978–87.
[18] Larsson EM, Alegret J, Kall M. Sutherland DS. Sensing characteristics of NIR localized surface plasmon resonances in gold nanorings for application as ultrasensitive biosensors. Nano Lett 2007;7:1256–63.

[19] Zhang X, Ma X, Dou F, Zhao P, Liu H. A biosensor based on metallic photonic crystals for the detection of specific bioreactions. Adv Funct Mater 2011;21:4219–27.
[20] Sagle LB, Ruvuna LK, Ruemmele JA, Van Duyne RP. Advances in localized surface plasmon resonance spectroscopy biosensing. Nanomedicine 2011;6:1447–62.
[21] Spadavecchia J, Barras A, Lyskawa J, et al. Approach for plasmonic based DNA sensing: amplification of the wavelength shift and simultaneous detection of the plasmon modes of gold nanostructures. Anal Chem 2013;85:3288–96.
[22] Ando M, Kobayashi T, Iijima S, Haruta M. Optical CO sensitivity of Au-CuO composite film by use of the plasmon absorption change. Sens Actuators B 2003;96:589–95.
[23] Sirinakis G, Siddique R, Manning I, Rogers PH, Carpenter MA. Development and characterization of Au-YSZ surface plasmon resonance based sensing materials: high temperature detection of CO. J Phys Chem B 2006;110:13508–11.
[24] Larsson EM, Langhammer C, Zorić I, Kasemo B. Nanoplasmonic probes of catalytic reactions. Science 2009;326:1091–4.
[25] Kreno LE, Hupp JT, Van Duyne RP. Metal-organic framework thin film for enhanced localized surface plasmon resonance gas sensing. Anal Chem 2010;82:8042–6.
[26] Rogers PH, Sirinakis G, Carpenter MA. Direct observations of electrochemical reactions within Au-YSZ thin films via absorption shifts in the Au nanoparticle surface plasmon resonance. J Phys Chem C 2008;112:6749–57.
[27] Tittl A, Mai P, Taubert R, Dregely D, Liu N, Giessen H. Palladium-based plasmonic perfect absorber in the visible wavelength range and its application to hydrogen sensing. Nano Lett 2011;11:4366–9.
[28] Tittl A, Kremers C, Dorfmüller J, Chigrin DN, Giessen H. Spectral shifts in optical nanoantenna-enhanced hydrogen sensors. Opt Mater Express 2012;2:111–8.
[29] Strohfeldt N, Tittl A, Giessen H. Long-term stability of capped and buffered palladium-nickel thin films and nanostructures for plasmonic hydrogen sensing applications. Opt Mater Express 2013;3:194–204.
[30] Anker JN, Hall WP, Lyandres O, Shah NC, Zhao J, Duyne RPV. Biosensing with plasmonic nanosensors. Nat Mater 2008;7:442–53.
[31] Peng W, Liang Y, Li L, Liu Y, Masson JF. Generation of multiple plasmon resonances in a nanochannel. IEEE Photon J 2013;5:4500509.
[32] Zentgraf T, Zhang S, Oulton RF, Zhang X. Ultranarrow coupling-induced transparency bands in hybrid plasmonic systems. Phys Rev B 2009;80:195415.
[33] Whittaker DM, Culshaw IS. Scattering-matrix treatment of patterned multilayer photonic structures. Phys Rev B 1999;60:2610–8.
[34] Tikhodeev SG, Yablonskii AL, Muljarov EA, Gippius NA, Ishihara T. Quasiguided modes and optical properties of photonic crystal slabs. Phys Rev B 2002;66:045102.
[35] Linden S, Kuhl J, Giessen H. Controlling the interaction between light and gold nanoparticles: selective suppression of extinction. Phys Rev Lett 2001;86:4688–91.
[36] Christ A, Tikhodeev S, Gippius NA, Kuhl J, Giessen H. Waveguide-plasmon polaritons: strong coupling of photonic and electronic resonances in a metallic photonic crystal slab. Phys Rev Lett 2003;91:183901.
[37] Underwood S, Mulvaney P. Effect of the solution refractive index on the color of gold colloids. Langmuir 1994;10:3427–30.
[38] Jensen TR, Duval ML, Kelly KL, Lazarides AA, Schatz GC, Van Duyne RP. Nanosphere lithography: effect of the external dielectric medium on the surface plasmon resonance spectrum of a periodic array of silver nanoparticles. J Phys Chem B 1999;103:9846–53.
[39] Nau D, Schönhardt A, Chigrin DN, Kroha H, Christ A, Giessen H. Polariton bandstructure of disordered metallic photonic crystal slabs. Phys Stat Sol B 2007;244:1262–9.
[40] Tien PK. Light waves in thin films and integrated optics. Appl Opt 1971;10:2395–413.
[41] Gallinet B, Martin OJF. Influence of electromagnetic interactions on the line shape of plasmonic Fano resonances. ACS Nano 2011;5:8999–9008.
[42] Gallinet B, Martin OJF. Relation between near-field and far-field properties of plasmonic Fano resonances. Opt Express 2011;19:22167–75.
[43] Chen H, Xu N, Deng S, et al. Gasochromic effect and relative mechanism of WO_3 nanowire films. Nanotechnology 2007;18:205701.
[44] Nau D, Seidel A, Orzekowsky RB, Lee SH, Deb S, Giessen H. Hydrogen sensor based on metallic photonic crystal slabs. Opt Lett 2010;35:3150–2.
[45] Johnson PB, Christy RW. Optical constants of the noble metals. Phys Rev B 1972;6:4370–9.
[46] von Rottkay K, Rubin M, Wen SJ. Optical indices of electrochromic tungsten oxide. Thin Solid Films 1997;306:10–6.
[47] Christ A, Linden S, Zentgraf T, et al. Optical properties of planar metallo-dielectric photonic crystals. Wiley-VCH, 2004:85–108.